Geophys. J. Int. (2002) **149,** 95–105

Mapping brittle fracture zones in three dimensions: high resolution traveltime seismic tomography in a granitic pluton

D. Martí,[1] R. Carbonell,[1] A. Tryggvason,[1] J. Escuder[2] and A. Pérez-Estaún[1]

[1]*Dept. Geofísica, C.S.I.C.-Inst. Ciencias de la Tierra "Jaume Almera",* 08028 *Barcelona, Spain*
[2]*Dept. Petrología y Geoquímica, Univ. Complutense,* 28040 *Madrid, Spain*

Accepted 2001 October 4. Received 2001 September 18; in original form 2000 November 20

SUMMARY

Fractured and altered zones within a granitic pluton are mapped in three dimensions by means of high resolution seismic traveltime tomography. The input traveltimes were picked from offset and azimuth variable vertical seismic profiles (OVSP) acquired in three boreholes and from seismic shot gathers of four CDP high resolution seismic reflection profiles recorded on the surface. For the OVSP data a hydrophone streamer placed in the boreholes recorded the acoustic energy generated (a signal with a frequency content between 15 to 150 Hz) by a Vibroseis truck at source points distributed every 30 m in a rectangular grid of 620 m by 150 m. The combination of borehole and surface seismic data resulted in an increase in the ray density of the shallow subsurface. The tomographic algorithm uses a variable model grid, with a finer grid spacing close to the surface were ray density is highest and the velocity variations are strongest. Therefore the resulting velocity models feature more detail at shallow levels. A simple and smooth starting velocity model was derived from *P*-wave velocity logs. Careful surface geological mapping, and borehole geophysical data, *P*- and *S*-wave velocity logs and Poisson's ratio depth functions, provided key constraints for a physically reasonable 3-D interpretation of the tomograms. The low velocity anomalies constrained by the tomographic images were interpreted as unconsolidated rock, fractures and altered zones which correlate with structures mapped at the surface or velocity anomalies identified in the logs. Subsequent resolution analysis revealed that the derived velocity model is well constrained to depths of 60 m.

Key words: fractures, seismic tomography, seismic velocities.

1 INTRODUCTION

The shallow subsurface is one of the highest providers of vital natural resources (for example, water, various food products, minerals) and could be the artificial host much of toxic and non-toxic waste. It is well known that groundwater flow is strongly influenced by the surface geology and the distribution of brittle fracture zones. Modern investigations have shown that predictions of contaminant transport require detailed information on the 3-D distribution of permeable volumes and of fracture zones within the shallow subsurface (Mair & Green 1981; Juhlin 1995; Juhlin *et al.* 2000).

The recent developments in high resolution seismic reflection techniques, e.g. source and receiver designs, innovative processing methods and computer simulations etc., have made the technique available to a broad spectrum of applications (Mair & Green 1981; Carswell & Moon 1989; Juhlin *et al.* 1991; Milkereit *et al.* 1992; Spencer *et al.* 1993; Milkereit *et al.* 1994; Juhlin 1995; Milkereit *et al.* 1996; Steeples *et al.* 1997; Steeples 1998; Morey & Schuster 1999; Juhlin *et al.* 2000). However, problems still exist when attempting to image 3-D structure in crystalline rock with 2-D acquisition geometries resulting in numerous out of plane reflections. In order to properly image these structures 3-D seismic data acquisition and processing is required.

A major concern in locating a nuclear waste site is the presence of hydraulically conductive subhorizontal fracture zones because they may have a major impact on water circulation patterns once waste has been deployed underground. These fracture zones are difficult to detect using geological mapping methods because they generally do not intersect the surface in the area being mapped. In addition, drilling and hydraulic testing often give data that are difficult to interpret because the rock mass is only sampled along lines. This may result in poor borehole to borehole correlation. Reflection seismics is a tool for integrating surface studies with borehole results in locating subhorizontal to gently dipping fracture zones, some of which may be hydraulically conductive. Because of the large amount of parameters that need to be known when considering a nuclear waste disposal site, it is very important that the seismic image obtained has the highest degree of accuracy possible. The geometry of the subhorizontal events on a seismic image need to be confirmed as truly being subhorizontal by shooting a large amount of intersecting cross-lines or,

preferably by acquiring 3-D data. Fracture zones in crystalline rocks have different physical properties than the surrounding host rock. The presence of cracks, altered material and fluids (water) results in lower seismic velocities in the fractured zones than in the fresh unfractured rock (Moos & Marion 1994). Therefore, a carefully designed seismic tomography experiment should be able to map velocity differences within the crystalline rock body. Shallow seismic tomography has been successful in identifying shapes and sizes of colluvial wedges (Morey & Schuster 1999). Theoretical calculations and high resolution seismics (Kanasewich *et al.* 1983; Holliger & Robertsson 1998) have shown that the shallow subsurface is where most of the wave conversions take place and where seismic velocities have the largest variations. This complex seismic wavefield in the shallow subsurface makes high resolution seismic reflection images difficult to interpret. 3-D high resolution seismic reflection surveys are very costly, require a considerable field effort and are very expensive with existing technology.

As part of the Spanish Nuclear waste Management Company's Uranium mine restoration programme (ENRESA) a high resolution tomographic experiment was carried out in a test site in southwestern Spain in an old abandoned mine site (Fig. 1). The tomographic data acquisition experiment was part of a multigeophysical experiment with the main aim of testing and studying the resolving power of a broad variety of techniques for characterization of the shallow subsurface. The experiment included: detailed surface mapping, several intersecting seismic reflection profiles, borehole geophysics and, high resolution tomography. The first results of the geological mappings and geostatistics modelling have been reported elsewhere (Escuder-Viruete *et al.* 2001). For the tomography we designed a relatively low cost high resolution tomographic acquisition experiment in order to be able to map velocity differences between fresh unfractured rock and fractured and altered domains within a granitic pluton.

In the present study we address the seismic data acquisition, the algorithm development and the application of the high resolution tomography experiment. We also evaluate the performance of the tomographic algorithm using different types of data, traveltimes derived from surface acquired shot records and traveltime data derived from vertical seismic profiles.

2 GEOLOGICAL AND GEOPHYSICAL BACKGROUND

The Ratones mine is an old abandoned Uranium mine exploited between 1955 and 1975. It is located within the Albalá Granitic Pluton (Fig. 1) in the Variscan Iberian Massif (Julivert *et al.* 1966). The Albalá granitic pluton consists of a concentric zoned body elongated in the N–S direction with biotitic, porphyritic granites in the rim and fine-grained two-mica leucogranites in the core. Major and trace elements suggests that magmatic rocks form a continuous sequence ranging from granodiorites through granites, monzogranites to leucogranites (Gumiel & Campos 1993). Rb–Sr dating intrusives ages of 302 ± 4 Ma. Sn, W, P and U mineralization are present in dikes and are genetically related with the most differentiated leucogranitic hosted rocks (Reguillón *et al.* 1996). The mine exploited two subvertical dikes (27 and 27′) NNE–SSW oriented, with quartz, pechblenda, coffinite and black Fe–Mn oxides. The ore filled fractures are organized in a pattern, which is consistent with a late Variscan strike-slip tectonic regime that affected the area of the Albalá pluton (Castro 1986; Sanderson *et al.* 1991).

Surface geological mapping has revealed a complex network of faults and joints which are indicative of a complex deformation pattern (Fig. 1) (Escuder-Viruete *et al.* 2001). Two deformation events, during Tertiary times, generated brittle fractures in the Albalá pluton which are superimposed on ductile-to-brittle late Variscan structures. These brittle structures are subvertical and geometrically grouped in two sets: a sinistral NNE–SSW to NE–SW set and the conjugate dextral N–S set. Their slip-vector is indicative of strike-slip faults. The kinematics of both fault sets and palaeostress analysis suggest that the maximum stress (s1) was subhorizontal, NNE directed. The NNE–SSW to NE–SW trend is parallel to the direction of many late Variscan subvertical dikes and faults, which were reactivated as strike-slip faults. At outcrop scale, the strike-slip faults are defined by complex fault zones. These fault zones feature abundant subparallel joints, shears and minor faults, with relatively small (<1 m) horizontal throw. A second series of structures grouped dominantly in two conjugate sets: NNE–SSW sinistral and ENE–WSW dextral, reactivated Late-Variscan dikes and Alpine strike-slip faults. The thickness of individual fault zones can vary between 0.1 and 25 m, though narrow fault zones (<0.5 m) are more frequent. Some of the cores through fault zone rocks contain secondary U-mineralizations of gummite, autunite and torbernite, probably generated by U remobilization in the fluid-phase of the fault network, during the reactivation of late-Variscan dikes as Alpine strike-slip faults.

To establish a hydrogeological flow model, a well resolved and detailed 3-D image of the fracture network is needed. The main surface geological feature identified in the study area (700 m by 500 m) (Fig. 1) is: the North Fault (NF) located at its northern edge. This is a 5 to 20 m wide brittle fracture that approximately parallels a road. Perpendicular to this main feature are two subvertical dikes (dike 27 and 27′), the two dikes exploited by the Uranium mine. Towards the southern edge of the study area there is an oblique and broad fault zone labelled South Fault (SF) that splits into three branches towards the northeast. An oblique fault labelled 285 is located at the centre of the tomographic block and approximately parallel to profile RTNS006.

Geophysical borehole data were also acquired in the three boreholes located within the study area (Fig. 1). Physical properties as a function of depth such as *P* and *S* seismic wave velocities, and Poisson's ratio were estimated from this borehole measurements (Fig. 2). The logs depth sample rate is of 0.20 m and they display a high degree of detail which is not observed in the tomographic images. The borehole tool has very limited penetration which varies depending on the physical conditions of the borehole walls. Therefore, the log data only reflects the physical properties of the rock volume within a radius (<0.5 m) around the borehole because of the limited penetration. This measurement will be different from the physical properties measured by the seismic tomography. The traveltime tomography measures the physical properties averaged along the ray paths. Thus, we can estimate the resolution scale of the traveltime tomography in the order of approximately 10 m. There are also differences between the values of the seismic velocities determined from the logs and from the seismic tomography. It is well known that the velocities determined from seismic data are 10–15 per cent lower than the velocities determined from the logs. This is a cumulative effect of the frequency of the signal, the averaging process along the ray paths, and the sampling intervals. However, the large scale features determined by the seismic tomography are reflected by the log data. The borehole data features a resolution scale that is smaller than the scale of resolution of the tomography, nevertheless, it places important constraints when interpreting the tomographic images. In order to be able to correlate the large scale features of both data sets the logs

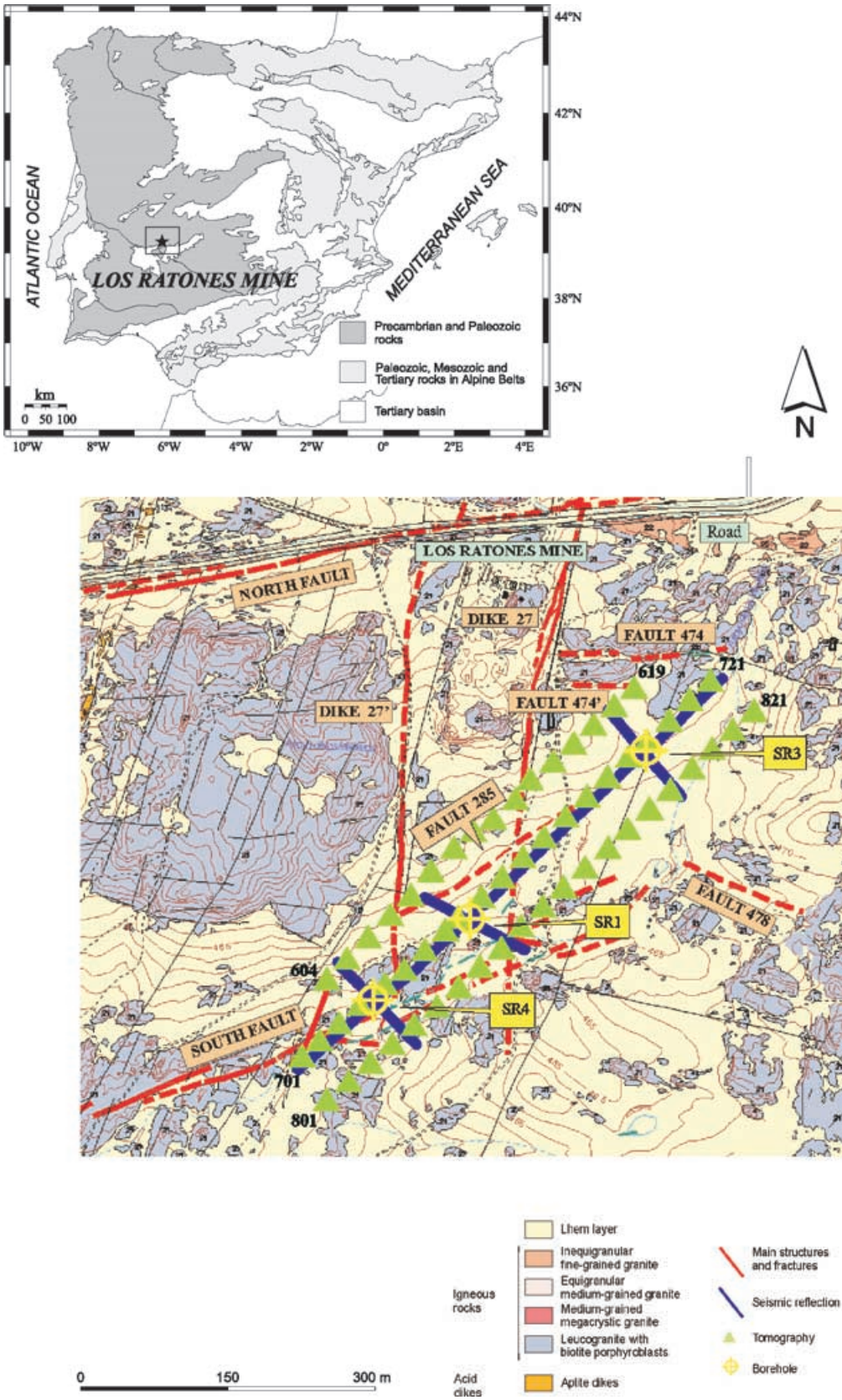

Figure 1. (a) Simplified sketch map of the geology of the Iberian peninsula indicating the location of the Ratones mine. (b) Structural map of the study area, indicating the main structures (dikes and fracture zones). The location of the high resolution seismic reflection profiles are indicated in blue. SR1, SR3 and SR4 indicate the location of the boreholes, the green triangles indicate the position of the source points of the Vibroseis tomographic experiment. The numbers next to the green triangles indicate the shot point number which increase from SW to NE.

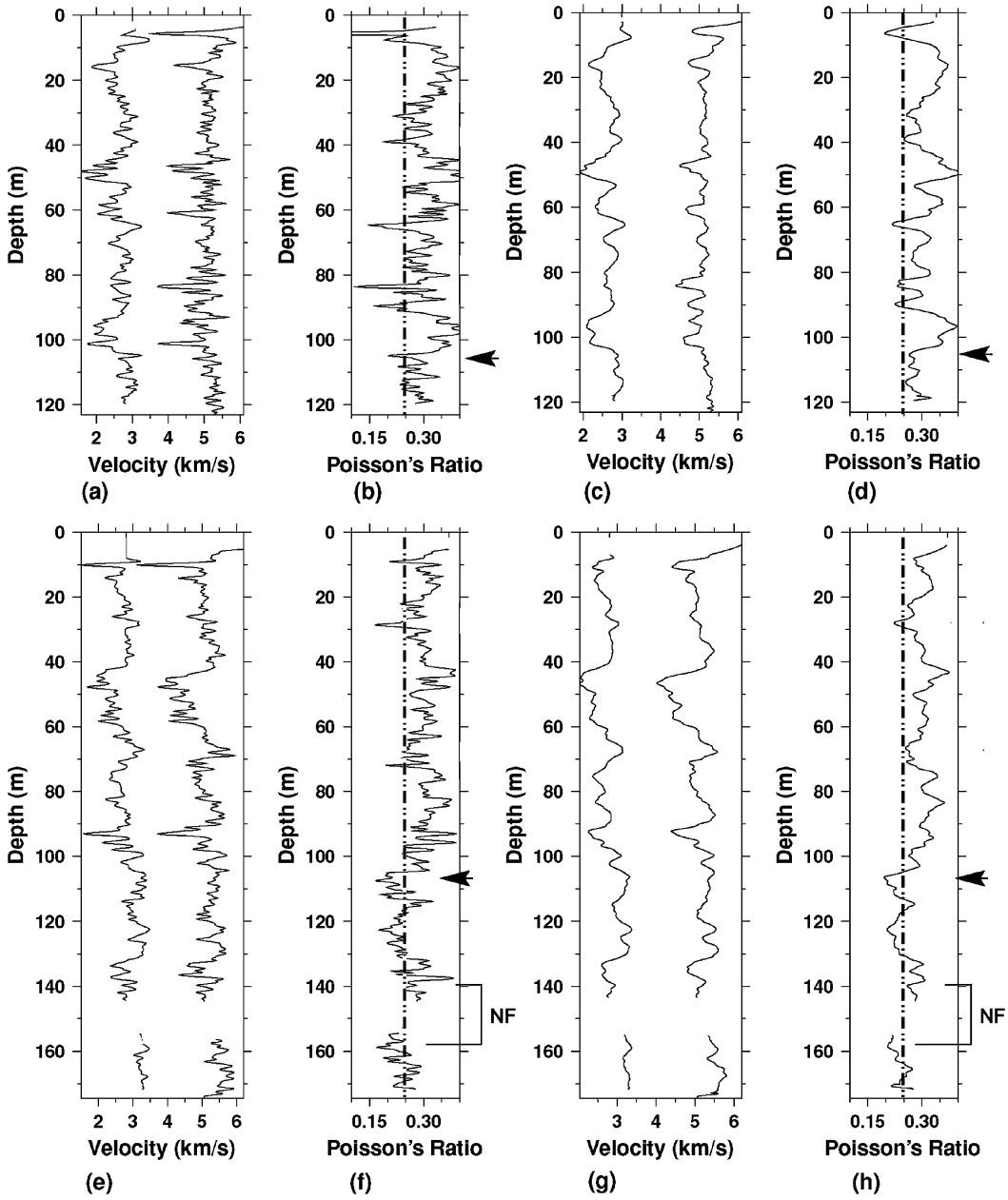

Figure 2. *P* and *S* wave velocity logs and Poisson's ratio (σ) depth functions for boreholes SR4 and SR3. (a) *P* and *S* wave velocity logs for borehole SR4. (b) σ for borehole SR4. (c) Average *P* and *S* wave velocity logs for borehole SR4. The values of the average velocity log at each depth have been obtained by averaging the values within a window 3 m wide around the target depth. (d) Average σ for borehole SR4. (e) *P* and *S* wave velocity logs for borehole SR3. (f) σ for borehole SR3. (g) Average *P* and *S* wave velocity logs for borehole SR3. (h) Average σ for borehole SR3. The location of the boreholes is indicated on the map of Fig. 1. The arrows emphasize the areas of the σ log where σ approaches the value of 0.25. $\sigma = 0.25$ is indicated in the σ logs by a discontinuous vertical line. NF marks the location of a wide brittle fracture zone interpreted to be the depth extrapolation of the North Fault indicated in Fig. 1 this interpretation is based on descriptions of the trace of the fault in the mine (Martínez & Ramirez 1966). The incompetent rock due to the brittle nature of the fracture NF, between 140 and 160 m depth in borehole SR3, resulted in unreasonable data and was edited from the log.

were smoothed by averaging the values over a 3 m depth window (Fig. 2).

The average velocity for all three boreholes is approximately 5.3 km s^{-1} and 2.8 km s^{-1} for the *P* and *S* waves respectively, a trend of increasing velocity with depth. For example: the top 50 m of borehole SR3 features average velocities of 5.2 and 2.8 km s^{-1} for *P* and *S* waves respectively, while for the bottom 50 m the average *P* and *S* waves are of 5.5 and 3.1 km s^{-1} respectively (Fig. 2). For the Poisson's ratio (σ) the opposite effect is observed. The average σ tends to decrease with increasing depth. The average value of σ for SR3 is 0.3 for the first 100 m while it decreases to approximately 0.25 for the bottom 60 m of the borehole. In more detail, SR3 displays three depth intervals where σ decreases close to 0.25 these are at approximately 30, 70 and 105 m which probably correspond to fresh unfractured zones. Although less prominent, similar effects can be detected in borehole SR4 (Fig. 2). Above 110 m σ features high values <0.3, indicating relatively thick bands of fractured rock, at approximately 20, 50 and 100 m, beneath 110 σ approaches

Table 1. Acquisition parameters for the four seismic reflection profiles. The traveltime picks of the first arrivals of the shot gathers were used in the tomographic inversion.

Profile	Length	Receiver interval	Shot interval	Num. of shots	Num stations
RTNS006	600 m	5.0 m	5.0 m	144	120
RTNS007	120 m	2.5 m	2.5 m	49	48
RTNS008	120 m	2.5 m	2.5 m	48	48
RTNS009	120 m	2.5 m	2.5 m	48	48

values close to 0.25 suggesting fresh unfractured rock. These features are emphasized once the logs are averaged (Fig. 2) over a few metres. These data were very useful in two ways as they were used to design a starting model and they constitute an asset for the physical interpretation of the resulting tomograms.

3 DATA ACQUISITION

The tomographic algorithm uses the first arrivals of seismic shot records and the precise location (x, y, z) of the sources and receivers. The target was a rectangular area around three boreholes (Table 1) of approximately 640 by 150 m (Fig. 1). Within this rectangular area 4 high resolution seismic reflection surface profiles were acquired (Fig. 1). For the high resolution seismic reflection surface profiles a 48 channel Bison seismograph was used. An 8 kg sledge hammer was used as a source, further details on the recording parameters are specified in Table 2. The source and receiver points were surveyed by a topographic crew who provide an accuracy of, approximately, 0.25 m. The travel times of the first arrivals were automatically picked by a refraction statics programme from the PROMAX seismic processing package (Land-Mark). The source and receiver locations were extracted from the trace headers of the SEGY formatted seismic traces.

A second data set which consisted of offset and azimuth variable vertical seismic profiles was acquired within the rectangular area (Fig. 1). A 22 Ton Vibroseis truck was used as a source. A 12 hydrophone streamer placed in the borehole recorded the acoustic energy generated by the Vibroseis truck. The Vibroseis truck vibrated in the nodes of a grid (Fig. 1) which consisted of 3 parallel lines one intersecting all the boreholes and the other two 60 m to each side of the central one. In each location the Vibroseis truck generated two sweeps with frequencies between 15 and 150 Hz with a time delay such that the 50 Hz electronic (ambient) noise was suppressed by a stacking procedure. Each shot was recorded by a 12 hydrophone streamer with a 4 m distance between hydrophones. Because of the depth of SR3, and SR4 these boreholes need to be surveyed twice. For example, SR3 was surveyed once between 12 m and 56 m depth and the second time between 60 m and 104 m depth. The traveltime of the first arrivals was digitized with a traveltime picking programme from the Seismix Unix seismic processing package (Colorado School of Mines). The source position was obtained during the seismic acquisition while the receiver position, hydrophone location was estimated using the geometry of the borehole (dip, azimuth and depth).

Table 2. Main characteristics of the boreholes used for the acquisition of offset and azimuth variable vertical seismic data.

Borehole	Sampled depth range	Dip	Azimuth
SR1	10–140 m	30°	104°
SR3	10–70 m	10°	16°
SR4	10–120 m	20°	160°

Due to the very high signal to noise ratio, quality control was only performed, to avoid shot gathers recorded with wrong starting times due to electronic failures. Noisy traces in which the first arrival could not be identified were edited and not used for the inversion (Fig. 3).

4 METHODOLOGY

4.1 Tomographic algorithm

Seismic tomography is a widely used technique to determine 3-D velocity structure. In the literature there are well developed reviews of the methodology (Aki & Richards 1980; Nolet 1993; Thurber 1986). The algorithm used in this study is based on the method by Benz *et al.* (1996).

In order to avoid local minima which might result in physically unreasonable velocity models a realistic starting velocity model is required. The target area includes three boreholes which have been studied using a variety of borehole geophysics: sonic logs, borehole televiewer, etc. The sonic logs provide additional information to design a simplified and physically reasonable starting velocity model. A simple *P* wave velocity model can be derived from the smooth velocity logs (Fig. 2). An average velocity of 5300 m s^{-1} can be estimated for the first 100 m approximately. Below this depth an average velocity of 5500 m s^{-1} are common in the velocity logs.

In order to evaluate the applicability of the tomographic inversion algorithm and to study its resolving power we have performed several inversions. In a first step only the 2,784 first arrivals traveltimes of the VSP's were used to obtain a *P* wave velocity model. The velocity model obtained in this inversion was then used as the starting model in a second run where the traveltime data of the VSP was combined with the traveltime picks of the surface recordings. The combined data set consisted on 15,295 travel times. In these two inversions the cell size was of $5 \times 5 \times 2$ m^3. The acquisition parameters of the surface seismic profiles resulted in a higher sampling of the shallow layers (down to 20 m). Because of this increase in the number of ray paths (cell sampling) more detail can be obtained near the surface if the cell size is decreased. The tomographic algorithm was modified so that it could handle different cell sizes in the same inversion. A third inversion was performed where the cell sized increased with increasing depth.

4.2 Resolution analysis and model assessment

The shallow subsurface accommodates the largest amount of heterogeneities with the highest velocity contrasts (Holliger & Robertsson 1998), it is where the seismic velocities are slowest and thus it is the area within the crust where high amplitude wave conversions occur (surface waves, Rayleigh, Love, etc.) (Kanasewich *et al.* 1983; Robertsson *et al.* 1996; Robertsson & Holliger 1997; Holliger & Robertsson 1998). Therefore, the tomographic algorithm requires an algorithm which is stable in the presence of sharp velocity contrasts.

The cell size is strongly dependent on the number of rays and their distribution within the velocity model. Therefore, uncertainty arises when deciding on the size of the cells because of the ability of the parameterization to represent structure and how well a parameter is

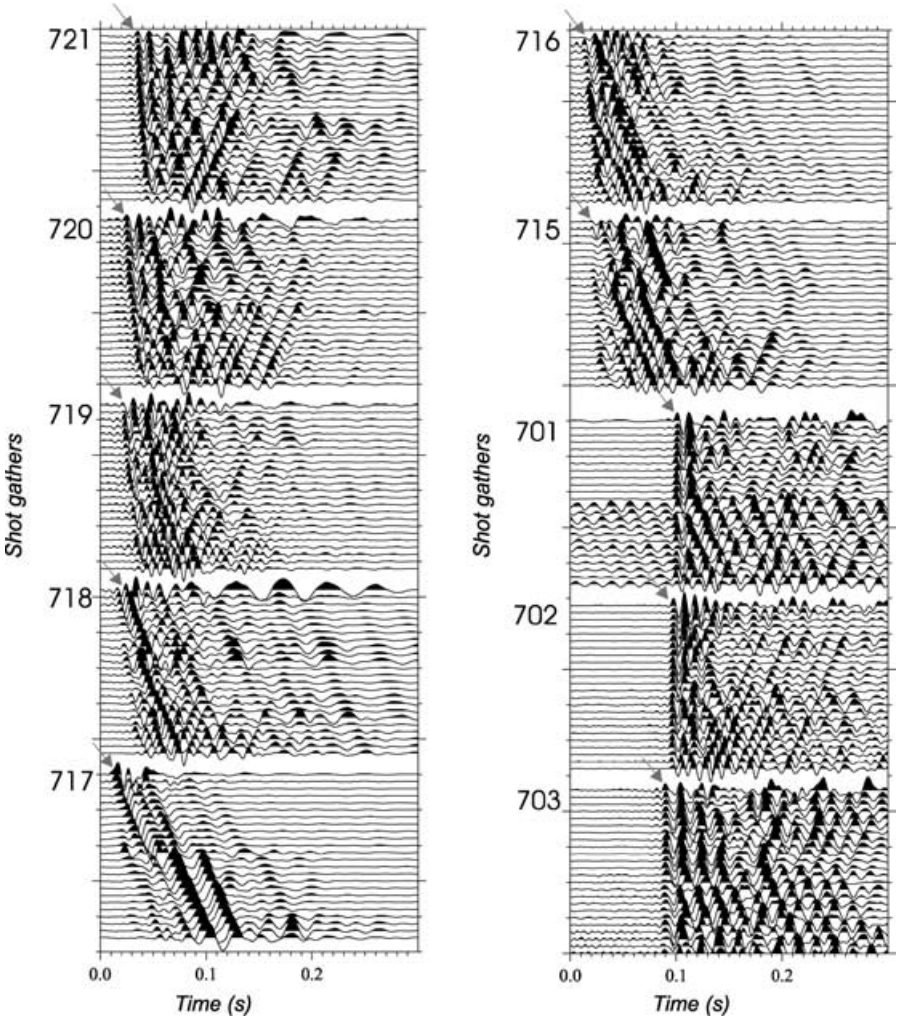

Figure 3. Vertical seismic record sections displaying the quality of the seismic data acquired by the streamer. These shot records where acquired in borehole SR3 from different source positions. The arrows marks the location of the first arrival onset. The number on top of each shot record identifies the source position (the numbers located next to the green triangles in Fig. 1).

constrained by the data. Because of the high resolution required in the present application, the most densely sampled model grid that did not produce an unstable solution is the preferred grid.

The model reliability was estimated by performing a series of synthetic tests which consisted in constructing checkerboard velocity models using the source and receiver geometry of the actual experiment. Synthetic traveltimes were calculated assuming a velocity model consisting of high and low velocity anomalies and estimated traveltime noise. The results from these tests reveal the areas of the model that are best constrained by the acquired data. Finally, to demonstrate the convergence of the inversion algorithm the value of the traveltime residuals was analyzed in order to assure that the traveltime residual would decrease in magnitude in each iteration, especially in the well constrained areas of the model.

5 DISCUSSION

In order to provide a reasonable explanation for the velocity anomalies we have reviewed the physical mechanisms that affect seismic velocities of rocks. From classical mechanics two types of seismic waves propagate through solid media, compressional and shear waves. The velocity of these waves is controlled by the density, bulk and shear modulus. Materials can be distinguished on the basis of the values of these parameters, however, these parameters vary with respect to their physical state, pressure, temperature, and composition. A comprehensive collection of seismic velocity measurements and the effects of composition as well as porosity and fluid saturation can be found in (Carmichael 1982) Porosity and pore contents has the strongest effect on seismic velocities, the shape of the pores is also a critical factor. Large aspect ratios (open cracks) influence the *P* wave velocities more (Nur 1987). Furthermore, mathematical models have been developed to study the effects of pores and cracks on seismic velocities (Watt *et al.* 1976; Berryman 1980; Norris 1985; Hudson 1980, 1994). These theoretical models take the shape of the pore into account and work under the assumption that the seismic wavelengths are much longer than the dimensions of the cracks or pores.

The critical porosity, which is the porosity above which the rock is no longer frame supported but fluid supported is controlled by the geometry of the pores. A crystalline rock with crack porosity may be fluid supported already at a porosity of a few per cent (Mukerji *et al.* 1995; Nur *et al.* 1998).

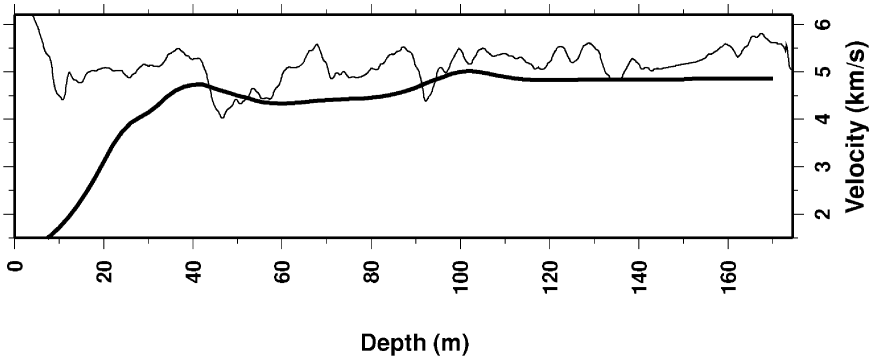

Figure 4. Comparison between the average *P* wave velocity derived from the log (thin line) and the *P* wave velocity as a function of depth in the vertical of SR3 derived from the Tomograms (bold line).

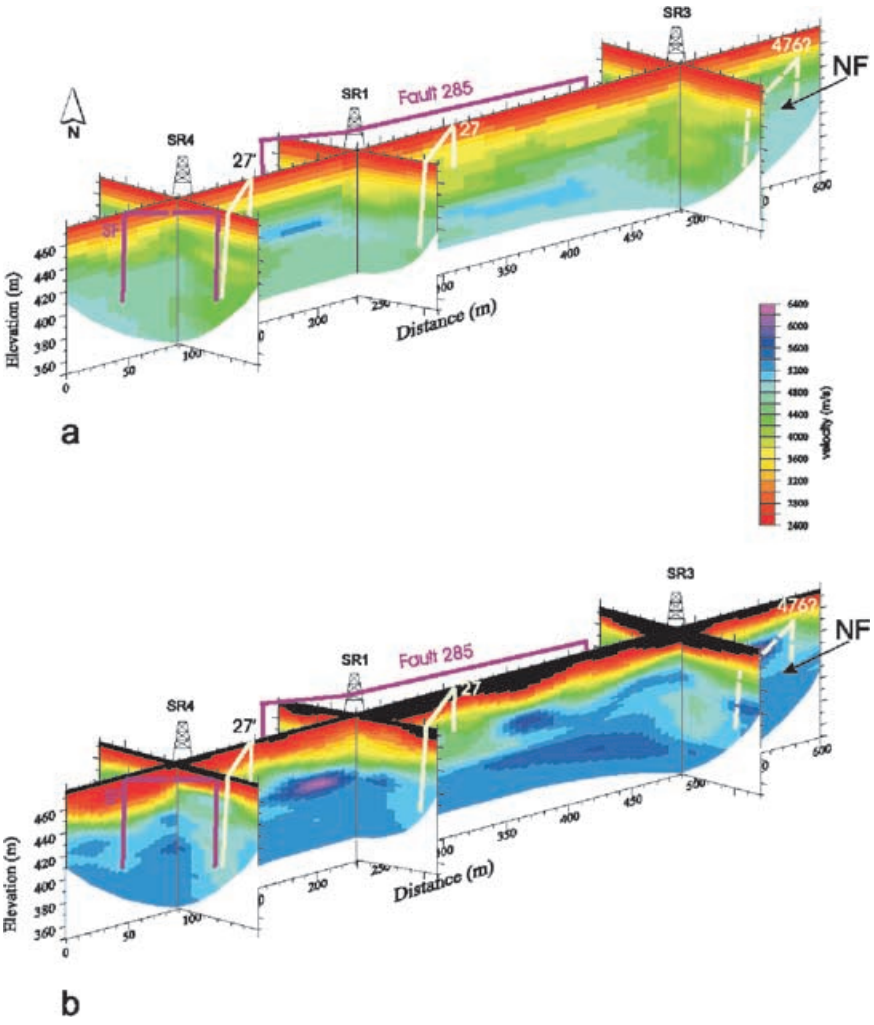

Figure 5. Tomographic images illustrating the velocity distribution within the block. The low velocity values are interpreted as altered or fractured zones within the granitic pluton. The location of the boreholes: SR1, SR3, and SR4 is also indicated. The slices shown coincide with the location of the surface seismic reflection profiles. The slice that intersects the three boreholes is RTNS006, the slices perpendicular to this one are at the location of the boreholes SR4, SR1, and SR3 are RTNS009, RTNS008 and RTNS007, respectively. (a) is the tomographic image of inverting the data recorded in the borehole (OVSP). (b) is the tomographic image that resulted from the inversion of the combined data sets (OVSP and surface seismic reflection data) and variable cell size. This latter result included the surface topography and therefore the black indicates areas above the surface. The exploited dikes (27 and 27′) can be identified as vertical low velocity anomalies to the east of boreholes SR4 and SR1. The geometry of two branches of the South fault can be identified intersecting the RTNS006 and RTNS009 profiles. A relatively low velocity anomaly to the south east of SR3 at approximately 90 m depth suggests the existence of a vertical brittle fracture zone labelled as 476 (see text for explanation).

When the porosity is unknown, statistical methods can provide upper and lower bounds for the values of the elastic moduli (Berge *et al.* 1992). Most laboratory data on porosity effects consist of ultrasonic measurements using a frequency range that differs from the one used in seismic exploration which can be between (1–500 Hz). When the pores are fluid filled their pressure may equilibrate with interconnected pores or fractures and more so with lower frequencies (Mukerji & Mavko 1994). For theoretically calculated moduli this effect is generally not considered, instead the Gassman relations (Gassman 1982) can be used to relate the dry moduli with the saturated ones. Material in the shallow subsurface is especially affected by porosity, the pore content and the degree of saturation. At depth, temperature is also an important controlling factor. As the present application deals with the shallow subsurface down to a depth of 150 m, temperature and pressure are not of critical importance. Another important simplification is that the characterization study deals with a single rock type as the study area is located within a granitic pluton. For granites and gabbros the decease in P wave velocities is less than 1 per cent per 100°C of temperature increase (Christensen & Mooney 1995). The velocity variations will most probably be due to porosity, fracture zones, chemically altered areas which will affect composition and the fluid content. Furthermore, only compressional waves will be considered (P waves). This is because only vertical component geophones were used in the surface seismic data acquisition, and only hydrophones were used in the borehole measurements. Although S waves are also recorded and present in the shot records, it is extremely difficult to identify precisely the traveltime of the first arrivals of S waves in these vertical component record sections. However, the effects of fractures and pore fluid content on S wave velocities is different than that on P wave velocities (O'Connell & Budiansky 1977). Fractures or unconsolidated rock are characterized by values of $\sigma > 0.25$ while fresh unaltered and consolidated rock features values close of $\sigma = 0.25$. The velocity and the Poisson's ratio logs provide a key for a physically reasonable interpretation of the velocity anomalies determined by the high resolution tomographic inversion. In the present study we are considering only isotropic models and the low P wave velocity anomalies will most probably be related to brittle fracture zones and altered rock volumes.

5.1 Geological interpretation

The velocity values determined by the tomography don't correlate one to one with the velocity values derived from the borehole logs this is mostly due to the differences in acquisition geometry, and instrumentation (the sampling intervals, resolution, frequency content of the source signal, ray path averaging, etc.). However, once both data sets have been smoothed in order to have similar resolution properties, the large scale structures, the main features, like the highs and lows are identifiable in both data sets (Fig. 4).

The Poisson's ratio measured in the boreholes down to 35–40 m is $\sigma > 0.25$, close to 0.33 this characterizes the surface layer as a weathered unconsolidated layer of granite (lehm cover) which is chemically altered and features high porosity. This correlates with the shallow low velocities (reddish colours in Fig. 5) of the velocity model determined by the inversion of the combined seismic data. This layer varies laterally, for example, considering the 3-D velocity model derived by the tomographic inversion, the isovelocity of 3500 m s^{-1} shows this lateral variability of the weathered unconsolidated rock. This isovelocity surface sinks (increases in depth) in the neighbourhood of fractures indicating an increase of the porosity

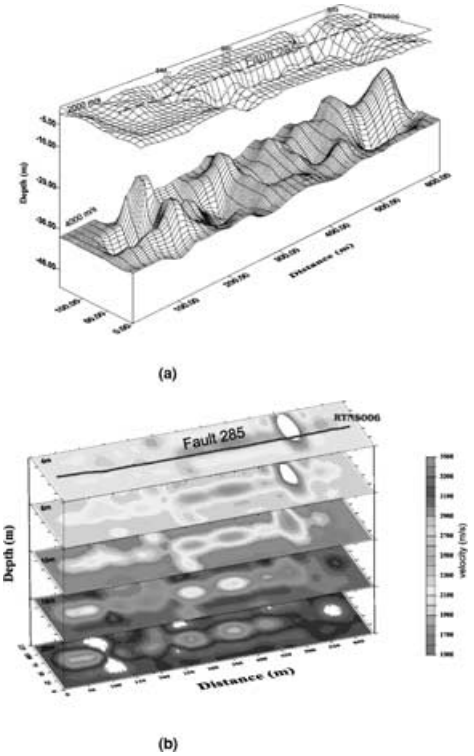

Figure 6. (a) Velocity isosurfaces for the velocities of 2000 m s^{-1}, 3500 m s^{-1}. Both isosurfaces reveal a prominent minima elongated in the NE–SW direction which coincides with the surface mapped fault 285. The isosurface of 2000 m s^{-1} represents the most unconsolidated surface weathered layer, while the isosurface of 3500 m s^{-1} which features an average depth of 35 m approximately coincides with the first minimum of σ for SR3 and SR4 (top most arrow in the σ logs of Fig. 2). The isosurface of 3500 m s^{-1} represents the transition to consolidated or fresh granite. The topography of this isosurface reveals a rhomboidal characteristic of the interference patterns of conjugate fractures. (b) Velocity slices at various depth the relatively low velocities indicate the geometry and location of fault 285.

(or fractures) (Fig. 6). Thus the thickness of the weathered unconsolidated layer of granite (lehm cover) varies laterally, being thicker along mapped fractures, for example along fracture 285 (Fig. 6). The low velocities imaged by the tomograms are probably due to fractured and altered granite (approximately, between 40 and 70 m). Because of the high porosity interpreted from the images this layer is probably hydraulically conductive (O'Connell & Budiansky 1977; Watt *et al.* 1976; Mukerji *et al.* 1995).

Beneath 70 m depth in average the fracturing decreases, σ values decrease to 0.25 (Fig. 2) and P wave velocity increases to 5300 m s^{-1} (Fig. 5). The fractures and the degree of alteration decreases with increasing depth as shown in the borehole logs by the decrease of σ which approaches values of 0.25 typical of consolidated rock. The relative increase in the velocity of the 3-D model (and logs) with depth reveals a decrease in the degree of fracturing and alteration. Because of the decrease in porosity these zones are probably not hydraulically conductive.

The tomographic images (Fig. 5) obtained in all the inversions feature the anomalies in almost the same location, however, when the combined data set was used higher resolution was obtained and the anomalies decrease in size. The low velocity anomalies correlate with the mapped brittle fractures. For example, the surface mapped faults SF, 285 and the exploited dikes 27′ and 27 all correlate with relatively low velocity anomalies. Because of this we postulated

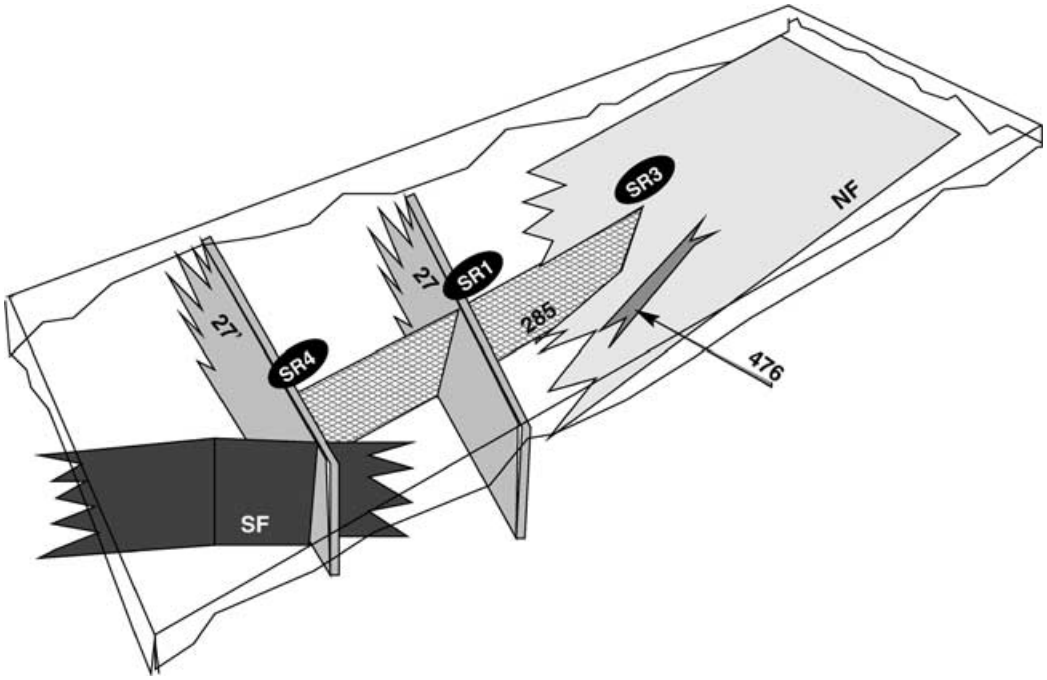

Figure 7. Sketch of the model with the most significant geological structures. NF North fault, SF South fault, Fault 285, Dykes exploited by the mine 27 and 27′, and the predicted fault 476. The location of the boreholes SR3, SR1 and SR4 is also indicated. The surface unconsolidated weathered layer determined from the tomograms is also indicated.

a fault 476 which has not been mapped on the surface. This low velocity anomaly intersects SR3 at approximately 90 m depth. At this depth the logs display a prominent low velocity anomalies for both P and S waves with $\sigma \approx 0.34$. In addition, the core has a high density of fracturing in this depth range. At the intersections of SF and dike 27′ and fault 285 and dike 27 the low velocity anomalies increase in width (Fig. 5).

Fig. 7 displays the most relevant geological structures identified in the tomographic images. If we follow the same procedure for other velocity values the velocity isosurfaces display an irregular topography. These isosurfaces feature a rhomboidal pattern revealing the configuration of a conjugate fracture pattern. Because of the smoothing constraints imposed to stabilize the inversion the thickness of the interpreted fracture or altered zones are probably overestimated.

5.2 Methodology and data resolution

The 3-D tomographic velocity model was obtained in a series of steps. In the first step only the OVSP data was used in the inversion. For this step the starting model was a simple and smooth velocity model derived from the velocity logs of the boreholes. This first step produced a model where the most prominent characteristic features were already resolved.

A second step consisted of inverting jointly the OVSP and the surface seismic data, the starting model was the one obtained in the previous step. The result had increased the resolution of the shallow structures (especially the unconsolidated, fractured and altered surface layer). The ray path diagrams (8) indicated that this shallow layer was over determined, therefore we could attempt to image even smaller anomalies by decreasing the size of the cells near the surface.

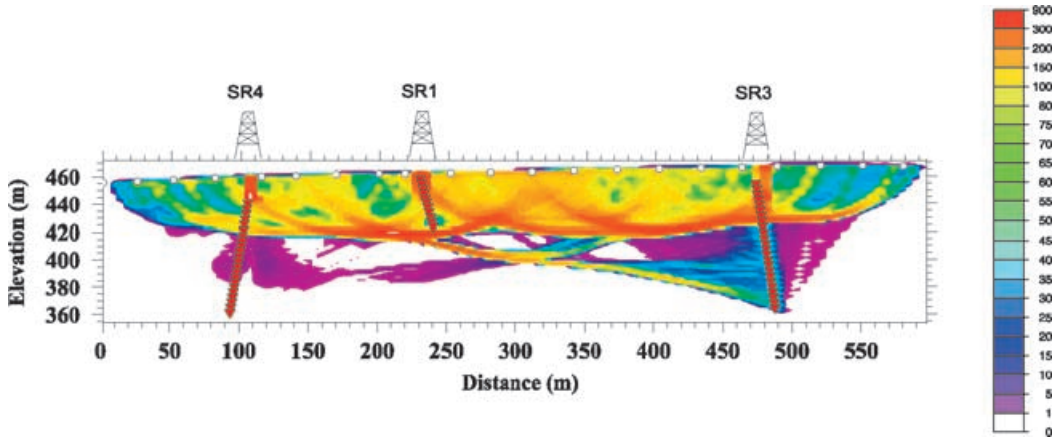

Figure 8. Ray path diagrams for a slice through the velocity model illustrating the cell sampling by the combined data set (surface recorded shot gathers and vertical seismic records).

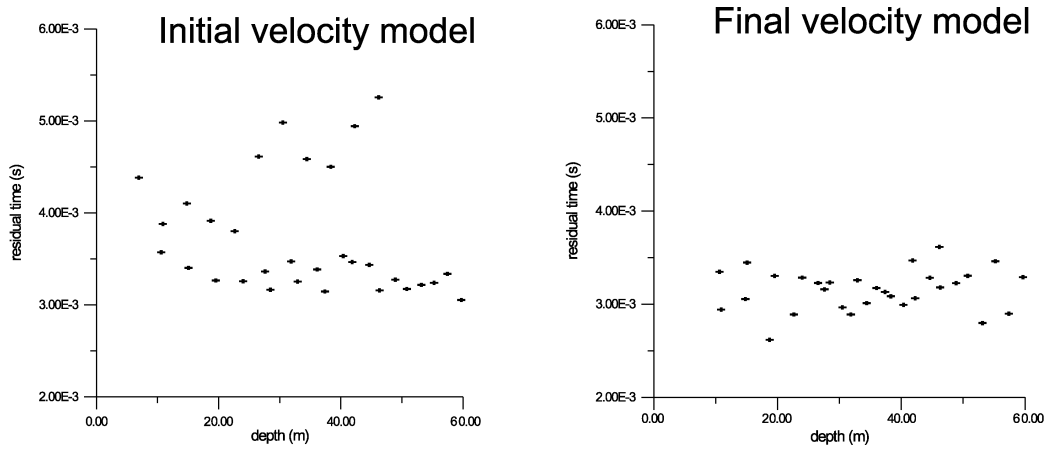

Figure 9. Traveltime residuals for the starting and final velocity models as a function of depth. The traveltime residual is the difference between the recorded traveltime and the traveltime computed by the forward modelling algorithm of the tomographic inversion scheme.

This increased the resolution of the shallower layers increasing the fidelity of the resulting model. This also changed the parameterization of the model and implied recoding of the inversion and forward modelling schemes of the tomographic algorithm. In the new scheme the size of the cells increased with depth. When choosing the size of the cells caution was taken in assuring that all cells where sampled by the same number of rays. Fig. 9 demonstrates the convergence of the inversion algorithm, the traveltime residual decreases in magnitude in each iteration, especially in the well constrained areas of the model. Finally, in order to constrained the well resolved parts of the model checker board test were performed (Fig. 10). This revealed that 3-D tomographic model was best resolved down to 60 m depth in average. Nevertheless, the ray path diagram (Fig. 8) reflects that in the neighbourhood of the boreholes, the structure is well sampled down to the bottom of the borehole and therefore the velocities determined within this volume are also physically meaningful.

The inverted velocity model features a low velocity anomaly that follows a fracture zone mapped by the surface geology (285 in Fig. 5). Although the fracture is indicated as a relatively thin structure in the geological map the low velocity anomaly is about 5–15 m wide. This difference in thickness is most probably due to the alteration (chemical and physical) that usually exists in the neighbourhood of fractures. This decreases the seismic velocities around the fractured volume. For example, the shape of the isovelocity contour of 2000 m s^{-1} deepens in the neighbourhood of the fault zone (Fig. 6). Water flow favours the chemical alterations in the granitic rock body. These chemical and physical alterations have been described by Escuder-Viruete *et al.* (2001).

6 CONCLUSIONS

The internal distribution of low velocity zones within a granitic pluton have been imaged by high resolution seismic traveltime tomography. The target consisted of a 3-D volume of 640 × 150 m × 172 m. For the tomographic study the first arrival traveltime picks from shot gathers of surface seismic reflection profiles were combined with the first arrival travel times of offset and azimuth variable vertical seismic recordings. These data provided a well constrained 3-D velocity model down to 60 m depth. The tomographic images have been interpreted with the aid of careful surface geological mapping, *P*-wave and *S*-wave velocity logs and Poisson's ratio depth functions. These data provide evidence for the interpretation of the relatively low velocity anomalies as fractured and chemically altered rock volumes. The tomograms provide a 3-D mapping of the fracture zones within the crystalline rock body. The derived models are smooth and the thickness of the fractured are probably overestimated, nevertheless, the tomograms constrain: the depth extend of a vertical fault, the topography of the base of an unconsolidated surface layer, and volumes of fresh unfractured rock. High resolution tomography is an efficient tool for imaging a hydraulically conductive network within crystalline rock. This knowledge is mandatory for environmental assessment, and site characterization.

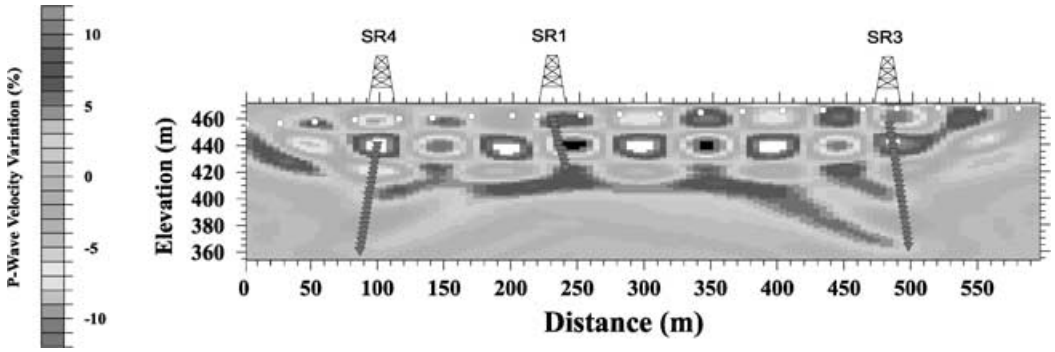

Figure 10. Checkerboard test with cell sizes of 20 × 50 m which revealed the well resolved areas of the model in order to identify the physically significant velocity anomalies. This image indicates that the velocity model is well constrained down to a depth of 60 m.

ACKNOWLEDGMENTS

We wish to thank ENRESA for making this high resolution experiment possible and supporting our research. T. Teixidor and the Servei Geological de Catalunya provided the instrumentation and field assistance. Comments by M. Fernandez, M. J. Jurado, J. Schön and two anonymous reviewers help improved this manuscript. Partial funding for this study was provided by CICYT grant BTE2000-0583-C02-01.

REFERENCES

Aki, K. & Richards, P., 1980. Quantitative Seismology: Theory and methods, Vol. 1, W. H. Freeman and company, New York.

Benz, H.M., Chouet, B.A., Dawson, P.B., Lahr, J.C., Page, R.A. & Hole, J.A., 1996. Three-dimensional P and S wave velocity structure of Redout Volcano, Alaska, *J. geophys. Res.,* **101,** 8111–8128.

Berge, P.A., Fryer, G.J. & Wilkens, R.H., 1992. Velocity-porosity relationships in the upper oceanic crust: theoretical consideration, *J. geophys. Res.,* **97,** 15 239–15 254.

Berryman, J.G., 1980. Long-wavelength propagation in composite elastic media I. Spherical inclusions and II. Ellipsoidal inclusions, *J. acoust. Soc. Am.,* **68,** 1809–1831.

Carmichael, R.S., 1982. *Handbook of Physical Properties of Rocks,* Vol. II, CRC Press, Boca Raton.

Carswell, A. & Moon, W.M., 1989. Aplication of multioffset vertical seismic profiling in fracture mapping, *Geophysics,* **54,** 737–746.

Castro, A., 1986. Structural patter and ascent model in the central Extremadura Batholith, Hercynian Belt, Spain, *J. struc. Geol.,* **8,** 635–645.

Christensen, N. & Mooney, W.D., 1995. Seismic velocity structure and composition of the continental crust: A global view, *J. geopys. Res.,* **100,** 9780–9788.

Escuder-Viruete, J., Carbonell, R., Marí, D. & Pérez-Estaún, A., 2001. Two dimensional geostatistical modelling and prediction of the fracture system in the Albal granitic pluton, SW Iberian Massif, Spain, *J. struct. Geol.,* **23,** 2011–2023.

Gassman, F., 1982. Uber die elastizität poroser mediem, *Vier. der Natur Geselschaft,* **96,** 1–23.

Gumiel, P. & Campos, R., 1993. Contribución al conocimiento geológico y goquímico de los granitos de Albalá y Montánchez (Extremadura central) y su relación con las mineralizaciones de estaño y wolframio, *Geogaceta,* **13,** 57–61.

Holliger, K. & Robertsson, J.O.A., 1998. Effects of the shallow subsurface on upper crustal seismic reflection images, *Tectonophysics,* **286,** 161–170.

Hudson, J.A., 1980. Overall properties of a cracked solid, *Math. Proc. Camb. Phil. Soc.,* **88,** 371–384.

Hudson, J.A., 1994. Overall properties of a material with inclusions or cavities, *Geophys. J. Int.,* **117,** 555–561.

Juhlin, C., 1995. Imaging of fracture zones in the Finnsjön area, central Sweden, using the seismic reflection method, *Geophysics,* **60,** 66–75.

Juhlin, C., Lindgren, J. & Collini, R., 1991. Interpretation of seismic reflection and borehole data from Precambrian rocks in the Dala Sandstone area, Central Sweden, *First Break,* **9,** 24–36.

Juhlin, C., Palm, H., Müllern, C. & Wallberg, B., 2000. High resolution reflection seismic applied to detection of groundwater resources in glacial deposits, Sweden, *Geophys. Res. Lett.,* **27,** 1575–1578.

Julivert, M., Fontboté, J.M., Ribeiro, A. & Nabais Conde, L.E., 1966. *Mapa tectónico de la Península Ibérica y Baleares,* 1:1000000, Inst. Geológico y Minero, Spain.

Kanasewich, E.R., Kelamis, P.G. & Abramovici, F., 1983. Exact seismograms for a point force, *Geophysics,* **48,** 1421–1427.

Mair, J. & Green, A.G., 1981. High resolution seismic reflection profiles reveal fracture zones within a homogeneous granite batholith, *Nature,* **294,** 439–442.

Martínez, A. & Ramirez, E., 1966. El yacimiento uranífero de Los Ratones, Albalá (Cáceres), *Bolteín Geológico y Minero,* **41,** 1–28.

Milkereit, B., Reed, L. & Cinq-Mars, A., 1992. High frequency reflection seismic profiling at Les Mines Sebaie, Quebec, *Curr. Res., Geol. Surv. Can.,* **92-1E,** 217–224.

Milkereit, B., Green, A.G., Wu, J., White, D. & Adam, E., 1994. Integrated seismic and borehole geophysic studies of the Sudbury Igneous Complex, *Geophys. Res. Lett.,* **21,** 931–934.

Milkereit, B., Eaton, D., Wu, J., Perron, G., Salisbury, M., Berrer, E.K. & Morrison, G., 1996. Seismic imaging of massive sulfide deposits: Part II. Reflection seismic profiling, *Ecin. Geol.,* **91,** 829–834.

Moos, D. & Marion, D., 1994. Morphology of extrusive basalts and its relatinship to seismic velocities in the shallow oceanic crust., *J. geophys. Res.,* **99,** 2985–2994.

Morey, D. & Schuster, G.T., 1999. Palaeoseismicity of the Oquirrh fault, Utah from shallow seismic tomography, *Geophys. J. Int.,* **138,** 25–35.

Mukerji, T. & Mavko, G., 1994. Pore fluid effects on seismic velocity in anisotropic rocks, *Geophysics,* **59,** 233–244.

Mukerji, T., Berryman, J., Mavko, G. & Berge, P., 1995. Differential effective medium modeling of rock elastic moduli with critical porosity constraints, *Geophys. Res. Lett.,* **22,** 555–558.

Nolet, G., 1993. Solving large linearized tomographic problems, in *Seismic Tomography: Theory and Practice,* pp. 248–264, eds Iyer, H.M. & Hirahara, K., Capman and Hall, London.

Norris, A., 1985. A differential scheme for the effective moduli of composites, *Mech. Mater.,* **4,** 1–16.

Nur, A., 1987. Seismic rock properties for reservoir descriptions and monitoring., in *Seismic Tomography,* pp. 203–237, ed. Nolet, G., D. Reidel Publishing Company, Dordrecht.

Nur, A., Mako, G., Dvorkin, J. & Galmudi, D., 1998. Critical porosity: A key to relating physical properties to porosity in rocks, *Leading Edge,* **17,** 357–362.

O'Connell, R.J. & Budiansky, B., 1977. Viscoelastic properties of fluid saturated cracked solids, *J. geophys. Res.,* **82,** 5719–5735.

Reguillón, R., Arribas, A., Martín-Izard, A. & Mangas, J., 1996. Las mineralizaciones de U de la Carretona y Casa de Gallo enel granito de Albalá (Caceres), *Geogaceta,* **20,** 1598–1600.

Robertsson, J.O.A. & Holliger, K., 1997. Modeling of seismic wave propagation near the Earth's surface, *Phys. Earth planet. Inter.,* **104,** 193–211.

Robertsson, J.O.A., Holliger, K. & Green, A.G., 1996. Source-generated noise in shallow seismic data, *J. Environ. Engin. Geophys,* **1,** 107–124.

Sanderson, D.J., Roberts, S.P., McGowan, J. & Gumiel, P., 1991. Hercynian transpresive tectonics at the southern margin of the Central-Iberian Zone, West Spain, *J. geol. Soc. Lond.,* **148,** 893–899.

Spencer, C., Thurlow, G., Wright, J., White, D., Carrol, P., Milkereit, B. & Reed, L., 1993. A Vibroseis survey at Burchaus Mine in central Newfoundland, *Geophysics,* **58,** 154–166.

Steeples, D.W., 1998. Shallow seismic reflection section-introduction, *Geophysics,* **63,** 1210–1212.

Steeples, D.W., Green, A.G., McEvilly, T.V., Miller, R.D., Doll, W.C. & Rector, J.W., 1997. A workshop examination of shallow seismic reflection surveying, *The Leading Edge,* **16,** 1641–1648.

Thurber, C., 1986. Analysis methods for kinematic datqa from local earthquakes, *Rev. Geophys.,* **24,** 793–805.

Watt, J.P., Davies, G.F. & O'Connell, R.J., 1976. The elastic properties of composite materials, *Rev. Geophys.,* **14,** 541–563.